LAWRENCE
LIVERMORE
NATIONAL
LABORATORY

LLNL-JRNL-522418

High Pressure Melting Curve of TIn

S. T. Weir, M. J. Lipp, S. Falabella, G. Samudrala, Y. K. Vohra

January 9, 2012

Journal of Applied Physics

Disclaimer

This document was prepared as an account of work sponsored by an agency of the United States government. Neither the United States government nor Lawrence Livermore National Security, LLC, nor any of their employees makes any warranty, expressed or implied, or assumes any legal liability or responsibility for the accuracy, completeness, or usefulness of any information, apparatus, product, or process disclosed, or represents that its use would not infringe privately owned rights. Reference herein to any specific commercial product, process, or service by trade name, trademark, manufacturer, or otherwise does not necessarily constitute or imply its endorsement, recommendation, or favoring by the United States government or Lawrence Livermore National Security, LLC. The views and opinions of authors expressed herein do not necessarily state or reflect those of the United States government or Lawrence Livermore National Security, LLC, and shall not be used for advertising or product endorsement purposes.

High Pressure Melting Curve of Tin Measured using an Internal Resistive Heating Technique to 45 GPa

S.T. Weir*, M.J. Lipp*, S. Falabella*, G. Samudrala†, and Y.K. Vohra†

*Lawrence Livermore National Laboratory
Livermore, CA 94550 USA

†University of Alabama at Birmingham
Birmingham, AL 35124 USA

Abstract

The high pressure melting curve of tin was measured to 45 GPa using a designer diamond anvil cell with an integrated internal resistive heating element. Melting of the tin sample was detected by an abrupt increase in the electrical resistance of the sample, and also by a change in the slope of the electrical heating power versus temperature curve. The melting temperatures determined by these two methods are in good agreement with each other. We find that the melting temperature of tin tends to monotonically increase with increasing pressure and reaches a temperature of about 2000K at 45 GPa, in good agreement with previous theory and experiment.

Introduction

The carbon group of elements (group 14) is characterized by the tendency to form covalent sp^3 bonds, with the strength and stability of the bonds decreasing with increasing atomic number among its members of C, Si, Ge, Sn, and Pb. This tendency to form sp^3 bonds in turn leads to a preference for the tetrahedrally coordinated diamond-type structure in many of these elements, although Sn is only stable in this structure at low temperatures (α-Sn) and Pb is not stable in the diamond-type structure at all due to its 6s electronic energy level being so far below its 6p energy level because of relativistic effects [1]. Among the group 14 elements, Sn sits on a borderline with a very weak capability of forming stable sp^3 covalent bonds [2,3].

Under the application of pressure, there is a tendency for the outer s-state electrons in these elements to be promoted to the p-state along with a decreasing tendency to form sp^3 bonds [2]. These factors help drive a series of pressure-induced structural phase transitions in Sn. Sn at room temperature transforms from the β-Sn structure into another body-centered tetragonal (bct) structure at 9.5 GPa [4], and then to a body-centered cubic (bcc) structure starting at a pressure of about 40 GPa, but with a wide pressure range of phase coexistence between 40 GPa and 52 GPa [5,6]. At 157 GPa, the bcc phase transforms to a hexagonal close-packed (hcp) structure which remains stable up to at least 194 GPa [7].

Interestingly, characteristic signatures of sp^3 covalent bonding persist into the liquid phases of many of these group 14 elements. Neither liquid Si, nor liquid Ge, nor liquid Sn exhibit simple liquid metal behavior with the high coordination number of 10-11 nearest neighbors expected of simple liquid metals. Instead, liquid Si, Ge, and Sn all have relatively small nearest neighbor coordination numbers of 6-7, with evidence of a significant amount of covalent bonding character as seen by the local anisotropic tetrahedral order exhibited by these liquids [8,9]. Narushima, *et. al.* [9] found that the application of high pressures to liquid Sn tends to decrease its covalent bonding character and anisotropic structural features, but that these anisotropic features still persisted up to at least 20 GPa, the highest pressure reached in their experiments. Interestingly, this pressure in the liquid phase greatly exceeds the pressure at which solid crystalline Sn loses its anisotropic bonding character, which is at the β-Sn to bct structural phase transition at 9.5 GPa [9].

The high-pressure melting curve of Sn is an interesting subject for study in order to further clarify the role of sp^3 bonding in the high pressure liquid and solid phases of Sn. The melting curve of Sn has been studied using a variety of static methods to pressures of up to 14 GPa [10,11,12,13,14], and more recently by Schwager, et. al. [15] using a laser-heated diamond anvil cell to a pressure of 68 GPa and 2300K. In addition, dynamic shock-wave experiments on Sn by Mabire and Héreil [16] found evidence of incipient melting of Sn on the Hugoniot curve at a pressure of 49 GPa and a calculated temperature of 2300K. Finally, Bernard and

Maillet [17] calculated the Sn melting line up to 40 GPa by means of *ab initio* molecular dynamics (MD) simulations and found good agreement with the shock-wave experiments.

We report here on static pressure melting line experiments on Sn to 45 GPa using a diamond anvil cell and an internal resistive heating technique. In contrast to laser-heating experiments that typically rely on laser speckle motion to detect the onset of melting, we detect melting by means of *in situ* monitoring of the electrical resistivity of the sample as well as by monitoring the electrical power versus temperature behavior of the heater-sample assembly. We have previously demonstrated the robustness of this technique through melting line experiments on gold up to 21 GPa [18].

Experimental Technique

The high pressure samples in our experiments are heated to high temperatures by driving large electrical currents through thin-film tungsten heating elements directly fabricated onto the culets of designer diamond anvils [18]. Figure 1 shows a basic schematic of the design. First, a shallow circular cavity approximately 30 μm in diameter and 10 μm deep is etched into the center of the culet of a designer diamond anvil [19,20]. This cavity is then packed with fine alumina powder (Saint-Gobain, 0.5 μm and oven dried at 110 ˚C), which serves as a thermal insulating layer. A thin-film tungsten electrical heating element measuring about 20 μm long, 10 μm wide, and 0.5 μm thick is then fabricated on top of the thermal insulating layer by optical lithography and tungsten sputter deposition. After further lithography, an Sn sample measuring about 10 μm x 10 μm x 0.5 μm is then sputter deposited onto the tungsten heating element. The Sn sputtering target has a purity of greater than 99.998%. Although small inclusions from the argon sputtering gas are believed to be present in the sputtered metal film at less than the 1% level, since argon is inert and forms no known compounds with Sn this is not believed to affect the melting temperatures. In addition, the solubility of tungsten in liquid Sn is extremely low (just 0.001 at% W in liquid Sn at 2273K [21]), so the presence of tungsten is not expected to affect the melting temperature measurements. Finally, tungsten has no known structural phase transitions throughout the pressure–temperature range of our experiments [22]. Further details about this heating technique can be found in reference 18.

The diamond anvil cells were prepared with one anvil having an electrical heating element and the Sn sample, and the opposite anvil being a standard 1/3 carat anvil with a flat diameter of 300 μm. The gaskets were made of spring steel and indented to about 50 μm, and a 100-110 μm hole was then drilled in the center of the indentation. The gasket hole was filled and packed with fine, dried alumina powder and several tiny (≈10 μm) ruby spheres were placed close to the sample to

act as pressure markers. Pressure measurements were made by the ruby fluorescence method [23].

To perform an experiment, the sample pressure was first increased to the desired value, and then the temperature was gradually raised by increasing the voltage and current across the heating element by means of a current-limiting control circuit [18]. The melting of a metal and the resulting loss of its crystalline order is generally accompanied by a large increase in the metal's electrical resistivity, typically by a factor of about two [24]. This translates into a change in the electrical resistance of the heating element+sample assembly by about 5%, which is large enough to be clearly observable with our instrumentation. The temperature of the sample was measured using blackbody spectroradiometry by observing radiant emission from a 10 μm x 10 μm square region of the tungsten heating element corresponding to the location of the sample through the base of the designer diamond anvil. Our system was calibrated with a calibration lamp operating at 2684K, and also validated against a temperature tunable blackbody source from 750K to 1330K. Emission spectra from the high-pressure and –temperature tungsten heating element were fitted over a wavelength range of 550 nm to 700 nm (Figure 2). The emissivity of tungsten was assumed to be independent of wavelength, which is a good approximation to the measured zero-pressure emissivity of tungsten [25]. Ruby pressure measurements taken before heating, during heating, and after heating showed that the pressure of the sample chamber during heating increased by not more than about 1.0 to 1.5 GPa.

Thermal Gradients

Thermal gradients in the sample are known to be a concern when performing very high temperature experiments with diamond anvil cells. To ensure the highest quality data, it is desirable to have extremely uniform temperatures throughout the region of the sample being examined by the diagnostic probe. In our experiment, good temperature uniformity is achieved in the axial (thickness) direction because the thickness of the sample (<1 μm) is much less than the thicknesses of the alumina insulating layers on either side of the sample-heater assembly. We estimate that the "sample filling fraction", which is defined as the ratio of the sample thickness to the overall thickness of the sample plus the insulating layers and is an important parameter controlling axial temperature gradients [26], to be less than 0.1 at all pressures reached in our experiments. Finite-element 2D thermal simulations reveal that the temperature variation throughout the cross-sectional area of a 10 μm wide, 1 μm thick heating element including the sample is about 5% at a temperature of about 2000 ˚C [18], with nearly all of this 5% variation in temperature being due to the center-to-edge temperature gradient along the 10 μm width of the heating element.

To determine the temperature variation along the length of the approximately 20 μm long heating element, we performed an experiment in which

we took blackbody spectra at every few microns along the length. Figure 3 shows the results, with the gray region marking the approximate position of a 10 μm x 10 μm thin-film sample. The temperature varies by about 28K or about 2% throughout this central region.

Results and Discussion

The data collected in our experiments is summarized in Figures 4 and 5. Figure 4 shows a set of electrical heating power versus resistance data taken at different pressures, with the melting of the Sn samples giving rise to small but abrupt increases in the electrical resistances of the heating element+sample assemblies. At each pressure, the location of the abrupt resistance increase is marked by an arrow. For the experiment at the highest pressure of 44.8 GPa, two rather abrupt resistance increases were observed. We will discuss this particular observation further later in this section.

We also observed that the heater power versus temperature data usually showed a significant change of slope in the vicinity of the melting point identified by the abrupt change in electrical resistance. The heater power versus temperature data is shown in Figure 5, with the points at which the data undergo sharp changes in slope marked by dashed lines. Circumstantial evidence strongly suggests that these slope changes are related to sample melting since in all four of the cases in which a distinct change in slope could be observed, the temperatures at which the heater power versus temperature data changed slope agreed with the melting temperatures determined by abrupt resistance changes to within 30K (Table I). In the remaining two experiments, the temperature data points were sparser and a change in the slope of the heater power versus temperature data could not be clearly identified. A possible explanation for these slope changes is that when the Sn sample melts it diffuses or migrates into the surrounding alumina, thus decreasing the effectiveness of the thermal insulation surrounding the heating element and reducing the slope of the heater power versus temperature data (i.e., the heating element becomes less efficient in terms of the electrical power required to maintain a given temperature).

An interesting feature of our 44.8 GPa experiment was the presence of not one but two abrupt increases in the electrical resistance, one at a temperature of 1242K and another at 1996K (Fig. 4). The associated heater power versus temperature data taken during this same experimental run shows a clear change in slope at a temperature of 2026K, which suggests that the resistance increase at 1996K is related to sample melting and that the resistance rise at 1242K is due to some other cause. Since Sn undergoes a bct–>bcc structural phase transition in the vicinity of 44.8 GPa, the resistance rise at 1242K is very likely caused by a change in the resistivity of Sn at this phase transition.

Figure 6 summarizes our high-pressure melting data on Sn. Also shown in Figure 6 are the Sn melting data points from the *ab initio* molecular dynamics calculations of Bernard and Maillet [17], and the proposed solid-liquid coexistence region based on shock-wave experiments [27]. Our data are in fairly good agreement with previous laser-heating experiments on Sn using laser speckle motion as the melting diagnostic by Schwager, et. al. [15], although our measured melting temperatures for pressures above 30 GPa tend to be slightly below the melting temperatures measured by Schwager, et. al. (e.g., measured melting temperature at 44.8 GPa is approximately 200K lower). Temperature discrepancies of this amount may be due to the fact that the two experiments measured temperatures off of different types of metal surfaces (tin for Schwager, et. al., and tungsten for our experiments), and Sn and tungsten may have different wavelength dependencies to their emissivities under high pressures.

Acknowledgements

This work performed under the auspices of the U.S. Department of Energy by Lawrence Livermore National Laboratory under Contract DE-AC52-07NA27344. We thank Hyunchae Cynn for his helpful comments.

1. N.E. Christensen, S. Satpathy, and Z. Pawlowska, *Phys. Rev. B* **34**, 5977 (1986).
2. H. Katzke, U. Bismayer, and P. Tolédano, *Phys. Rev. B* **73**, 134105 (2006).
3. N.E. Christensen and M. Methfessel, *Phys. Rev. B* **48**, 5797 (1993).
4. J.D. Barnett, V.E. Bean, and H.T. Hall, *J. Appl. Phys.* **37**, 875 (1966).
5. H. Olijnyk and W. Holzapfel, *Journal de Physique* **45**, c8-153 (1984).
6. M. Liu and L. Liu, *High Temp. High Press.* **18**, 79 (1986).
7. A. Salamat, G. Garbarino, A. Dewaele, et. al., *Phys. Rev. B* **84**, 140104 (2011).
8. V. Petkov and G. Yunchov, *J. Phys. : Condens. Matter* **6**, 10885 (1994).
9. T. Narushima, T. Hattori, T. Kinoshita, A. Hinzman, and K. Tsuji, *Phys. Rev. B* **76**, 104204 (2007).
10. J.D. Dudley, and T.H. Hall, *Phys Rev.* **188**, 1211 (1960).
11. J.D. Barnett, R.B Bennion, and T.H. Hall, *Science* **141**, 1041 (1963).
12. J. Jayaraman, W. Klement, Jr., and G.C. Kennedy, *Phys. Rev.* **130**, 540 (1963).
13. A.I. Kingon, and J.B Clark, *High-Temp. – High Press.* **12**, 75 (1980).
14. B. Kiefer, T.S. Duffy, T. Uchida, and Y. Wang, "Melting of Tin at High Pressures", APS User Activity Report, 2002.
15. B. Schwager, M. Ross, S. Japel, R. Boehler, *J. Chem. Phys.* **133**, 084501 (2010).
16. C. Mabire and P.L. Heréil, in *Proceedings of the APS Conference on Shock Compression of Condensed Matter*, edited by M.D. Furnish, L.C. Chabildar, and R.S. Hixson (AIP, Melville, 1999), p. 93.
17. S. Bernard and J.B. Maillet, *Phys. Rev. B* **66**, 012103 (2002).
18. S.T. Weir, D.D. Jackson, S. Falabella, G. Samudrala, and Y.K. Vohra, *Rev. Sci. Instrum*. **80**, 013905 (2009).
19. S.T. Weir, J. Akella, C. Aracne-Ruddle, Y.K. Vohra, and S.A. Catledge, *Appl. Phys. Lett.* **77**, 3400 (2000).
20. S.T. Weir, H. Cynn, S. Falabella, W.J. Evans, C. Aracne-Ruddle, D. Farber, and Y.K. Vohra, *High Pressure Research* **31**, 191 (2011).
21. B. Predel, : *Sn-W (Tin-Tungsten)*. Madelung, O. (ed.). SpringerMaterials - The Landolt-Börnstein Database (http://www.springermaterials.com). DOI: 10.1007/10551312_2771
22. Tungsten has no pressure-induced structural phase transition at room temperature to at least 4 Mbar and no high temperature structural phase transition before melting at T=3683K. See A. L. Ruoff, H. Xia, H. Luo, and Y. K. Vohra, *Rev. Sci. Instrum.* **61**, 3830 (1990) ; A. L. Ruoff, J. Xia, and Q. Xia, *Rev. Sci. Instrum.* **63**, 4342 (1992).
23. H. K. Mao, J. Xu, and P. M. Bell, *J. Geophys. Res.* **91**, 4673 (1986).
24. A.M. Rosenfeld and M.J. Stott, *Phys. Rev. B* **42**, 3406 (1990).
25. The emissivity of tungsten has a slight wavelength dependence, with the emissivity linearly decreasing by about 5% from λ=550 nm to λ=700 nm. See R.C. Weast, *CRC Handbook of Chemistry and Physics, 60th Edition*, CRC Press Inc., Boca Raton, 1980, pp. E-381, E-394. Assuming that the emissivity of tungsten is wavelength independent causes the calculated temperatures to be shifted

downward by less than 4%. Since the actual emissivity of tungsten at high pressure is unknown, we accept the fact that there may be systematic errors in the measured temperatures in the range of about 5%.

26. B. Kiefer and T.S. Duffy, *J. Appl. Phys.* **97**, 114902 (2005).
27. J. Hu, X. Zhou, C. Dai, H. Tan, and J. Li, *J. Appl. Phys.* **104**, 083520 (2008); B. Schwager, M. Ross, S. Japel, R. Boehler, *J. Chem. Phys.* **133**, 084501 (2010).

Table I. Summary of the Sn melting temperature data. $T_M^{(R)}$ are the melting temperatures determined by abrupt changes in the electrical resistance, and $T_M^{(P\text{-}T)}$ are the melting temperatures determined by significant changes in the slope of the power versus temperature data. For the experiment at 44.8 GPa, two abrupt changes in the electrical resistance were observed, one at T=1242K and another at T=1996K, with the first change attributed to the bct–>bcc structural phase transition and the second change attributed to Sn melting.

P (GPa)	$T_M^{(R)}$ (K)	$T_M^{(P\text{-}T)}$ (K)
10.5	1276	not observable
20.2	1445	1455
26.5	1443	not observable
30.3	1747	1747
37.5	1701	1717
44.8	1242, 1996	2026

Figure Captions

Figure 1

Schematic diagrams of a microheater designer diamond anvil. (a) A side-view showing the designer anvil with a thin-film tungsten heating element and alumina thermal insulation layers above and below it. (b) A top-view of the microheater region. Several of the diamond encased electrodes are used to carry a large electrical heating current to the microheater while other electrodes are used to monitor the voltage drop across the heating element, thus enabling the precise measurement of the electrical power dissipated by the heating element + sample assembly. (c) A picture of the tungsten heating element at a pressure of 30 GPa and a temperature of approximately 2000K.

Figure 2

A blackbody spectrum taken from a tungsten heating element at a pressure of 37.5 GPa and a temperature of 1648K. The blackbody spectrum is plotted on a Wien's approximation plot of the logarithm of $I\,\lambda^5$ versus $1/\lambda$, where I is the intensity (in arbitrary units) and λ is the wavelength (in nm). The blackbody fit is shown as a red dashed line, with the measured temperature being proportional to the reciprocal of the negative slope.

Figure 3

Temperature profile along the length of the 20 μm long tungsten heating element. The blackbody spectrum at each point was taken over a 10 μm x 10 μm spot size. The gray region between x = +5 μm and x = -5 μm corresponds to the approximate position of the sample.

Figure 4

Electric heating power versus normalized resistance data for the tungsten heating element + Sn sample assembly at various pressures. Resistances are normalized to 1 at zero power, and data are offset on the vertical scale by 1 for each successively higher pressure. Arrows indicate abrupt changes in the resistance versus power data which are attributed to the melting of the Sn sample. For the experiment at 44.8 GPa, two sudden changes in the resistance were observed, one at 1242K and another at 1996K, with the first change attributed to the bct->bcc transition in Sn and the second change attributed to the melting of the Sn. The solid lines are guides to the eye.

Figure 5

Electrical heating power versus temperature curves taken at various pressures. Dashed lines indicate the points at which the curves show significant changes in slope and the corresponding temperatures are listed. No clearly identifiable slope changes were observed for the experiments at 10.5 GPa and 26.5 GPa, possibly because the data points were too sparse at these two pressures.

Figure 6

Summary of the melting temperature versus pressure measured for Sn in these experiments. Filled circles (•): our data. Asterisk(*) : possible bct->bcc transition. Empty diamonds (◊) : *ab initio* calculations (Ref. 17). Filled diamond (♦): shock-wave experiment (Ref. 16). Filled square: zero-pressure melting temperature of Sn (505K). The dashed lines indicate the estimated positions of the solid-to-solid phase transitions of tin according to the available data.

Figure 1

(a)

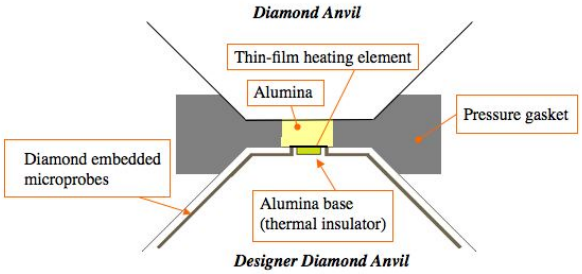
Diamond Anvil
Thin-film heating element
Alumina
Pressure gasket
Diamond embedded microprobes
Alumina base (thermal insulator)
Designer Diamond Anvil

(b)

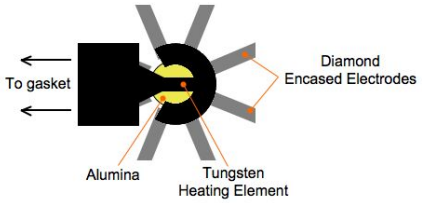
To gasket
Diamond Encased Electrodes
Alumina
Tungsten Heating Element

(c)

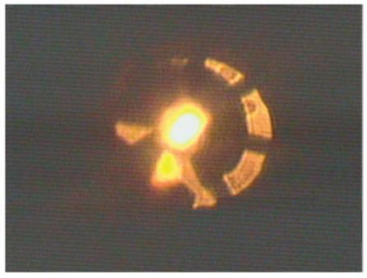

Figure 2

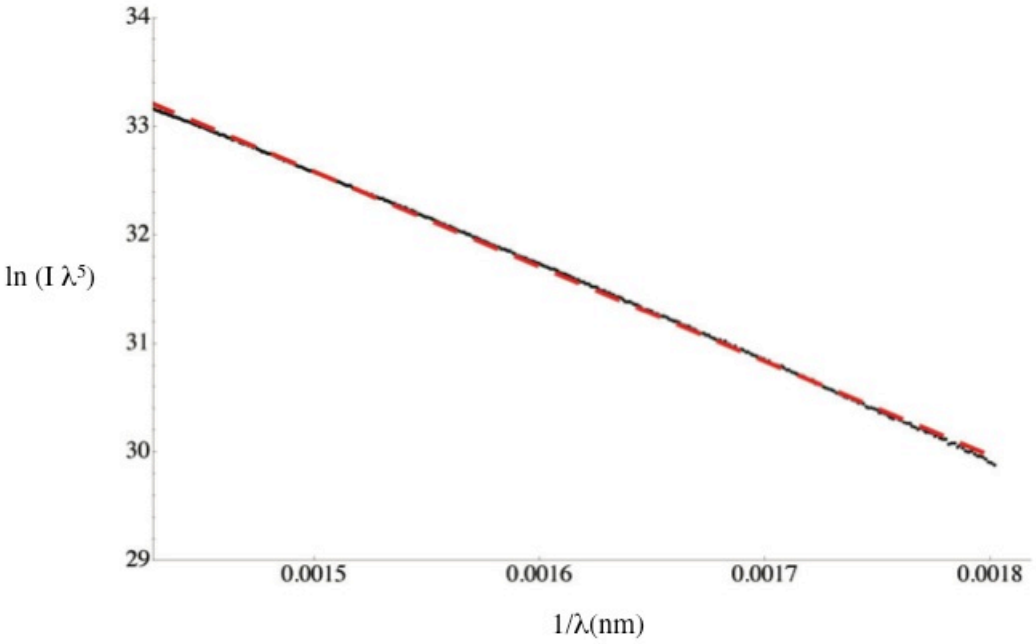

Figure 3

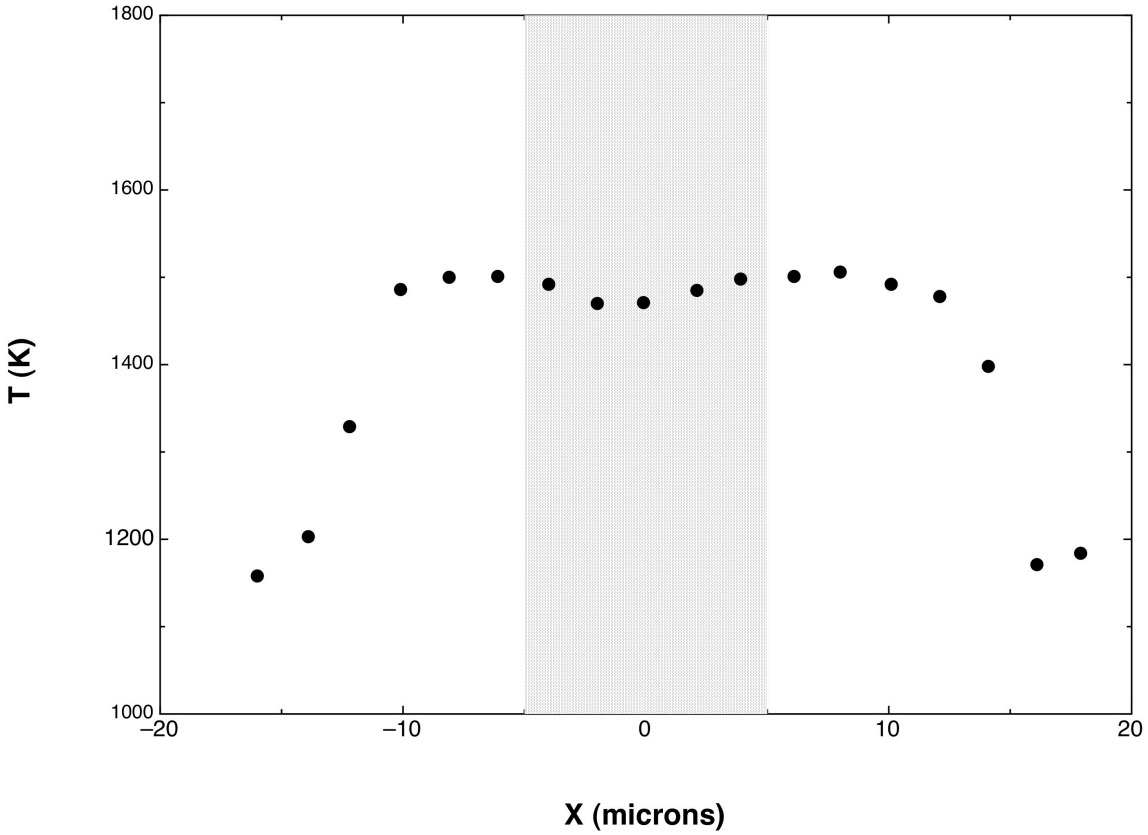

Figure 4

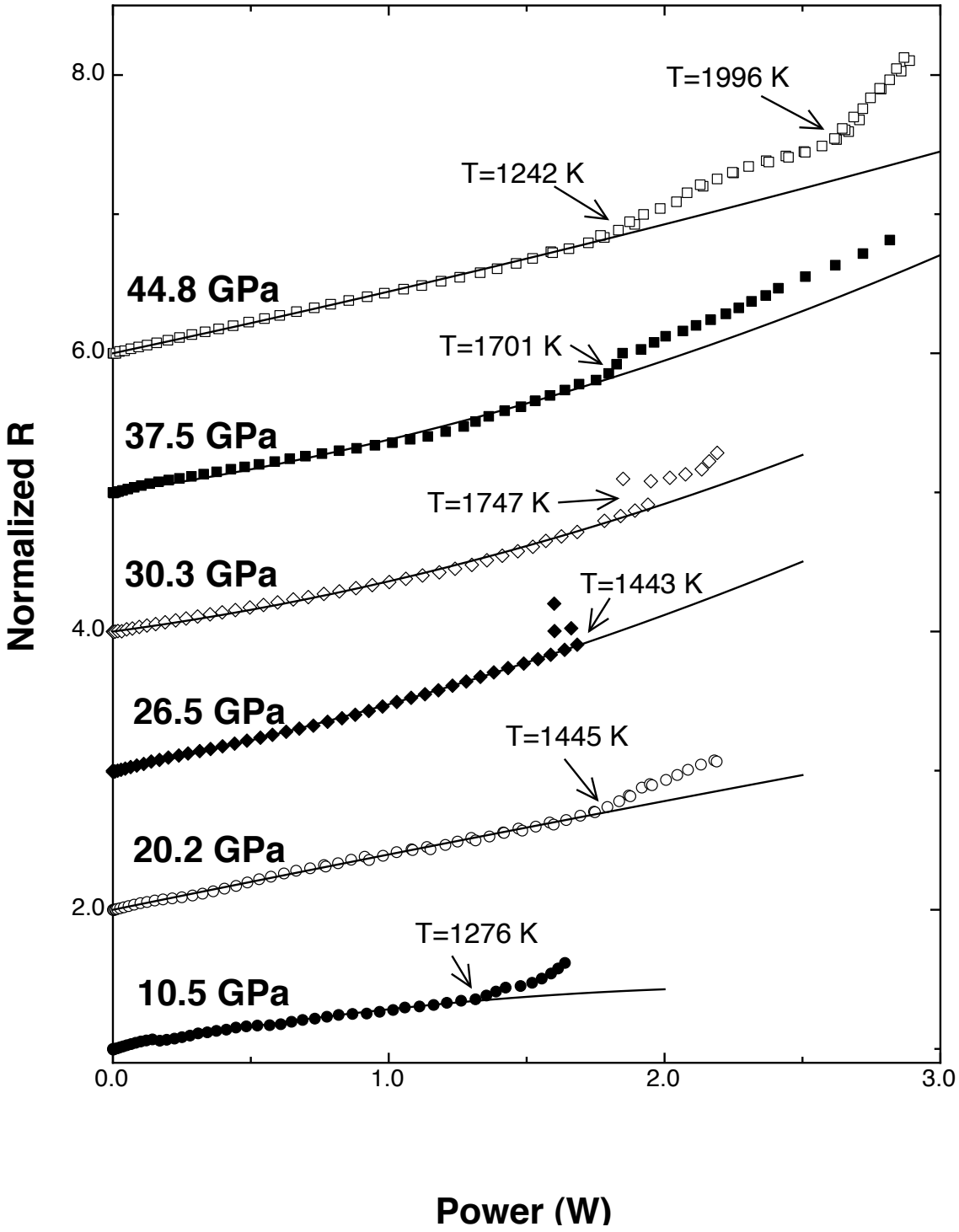
T=1996 K
T=1242 K
44.8 GPa
T=1701 K
37.5 GPa
T=1747 K
30.3 GPa
T=1443 K
26.5 GPa
T=1445 K
20.2 GPa
T=1276 K
10.5 GPa
Normalized R
Power (W)
8.0
6.0
4.0
2.0
0.0
1.0
2.0
3.0

Figure 5

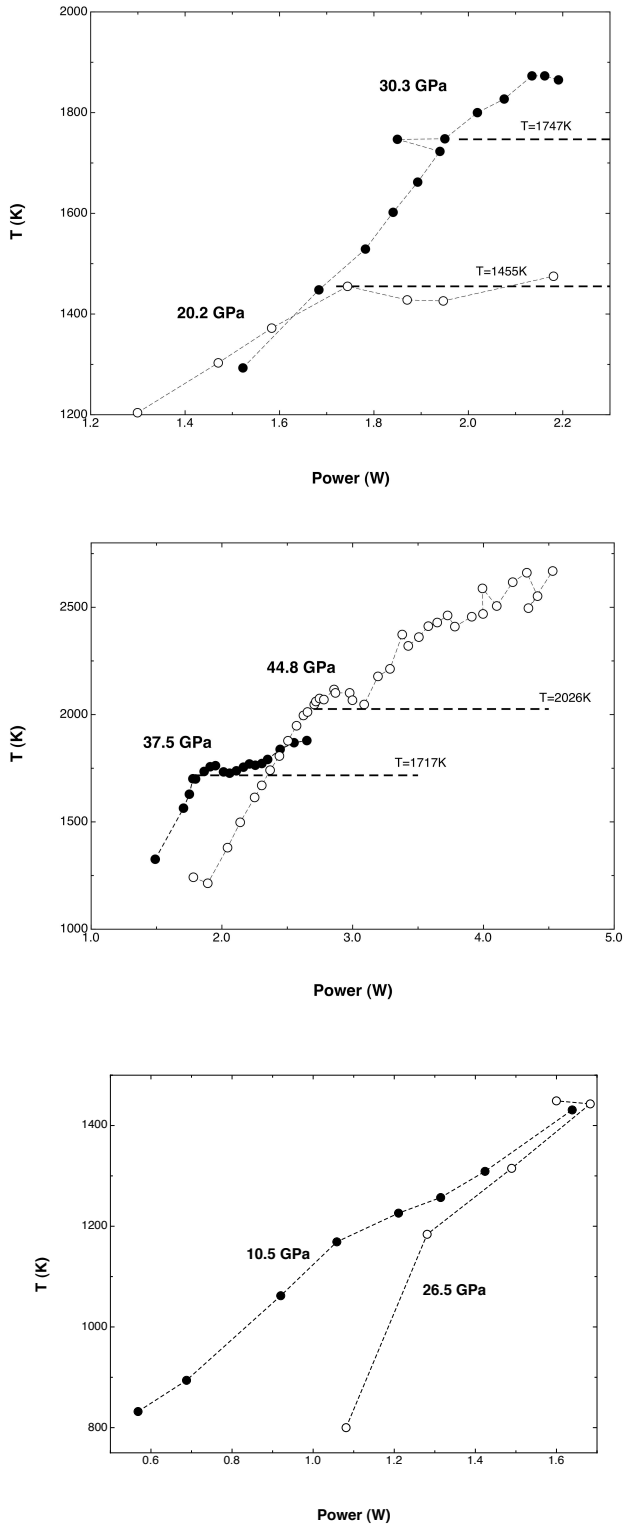
30.3 GPa
T=1747K
T=1455K
20.2 GPa
T (K)
Power (W)
44.8 GPa
T=2026K
37.5 GPa
T=1717K
T (K)
Power (W)
10.5 GPa
26.5 GPa
T (K)
Power (W)

Figure 6

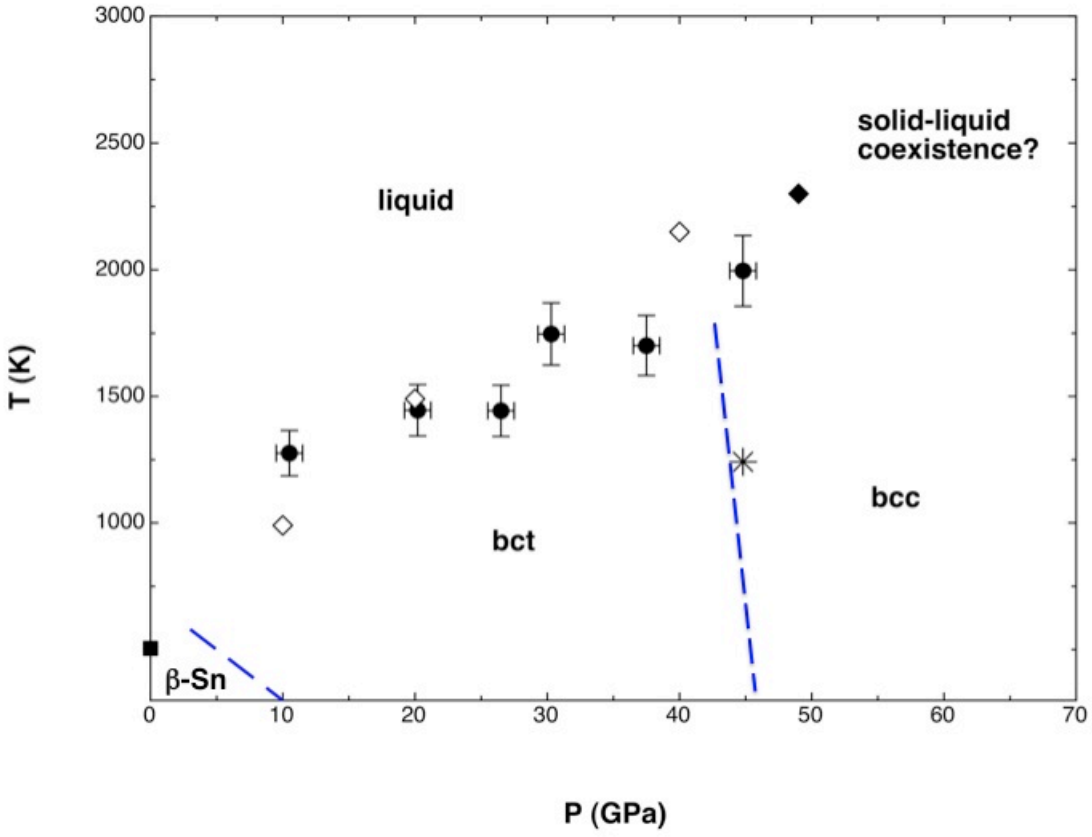
3000
2500
2000
1500
1000
T (K)
liquid
solid-liquid
coexistence?
bct
bcc
β-Sn
0
10
20
30
40
50
60
70
P (GPa)